Journal of Medical Ultrasonics
https://doi.org/10.1007/s10396-023-01282-2

ORIGINAL ARTICLE–PHYSICS & ENGINEERING

Speed-of-sound estimation in ultrasound propagation medium by considering size of target scatterer

Shohei Mori[1] · **Hiroshi Kanai**[1,2] · **Mototaka Arakawa**[1,2]

Received: 3 September 2022 / Accepted: 5 December 2022

Abstract

Purpose Accurate speed-of-sound (SoS) estimation in an ultrasound propagation medium improves imaging quality and contributes to better diagnosis of diseases. In conventional time-delay-based SoS estimation approaches studied by several groups, a received wave is assumed to be scattered from an ideal point scatterer. In these approaches, the SoS is overestimated when the target scatterer has a non-negligible size. In this paper, we propose the SoS estimation method that considers target size.

Methods In the proposed method, the error ratio of the estimated SoS using the conventional time-delay-based approach is determined from measurable parameters using the geometric relationship between the received elements and target. Subsequently, the SoS erroneously estimated using conventional estimation, assuming the ideal point scatterer as a target, is corrected by the determined estimation error ratio. To validate the proposed method, the SoS in water was estimated for several wire sizes.

Results The SoS in the water was overestimated using the conventional SoS estimation method, with a maximum positive error of 38 m/s. The proposed method corrected the SoS estimates, and the errors were suppressed to within 6 m/s, irrespective of the wire diameter.

Conclusion The present results demonstrate that the proposed method can estimate the SoS by considering the target size without using information on the true SoS, true target depth, and true target size, which is applicable to in vivo measurements.

Keywords Ultrasound · Speed of sound

Introduction

Medical ultrasound imaging is useful for observing biological tissues owing to its noninvasiveness and real-time performance. Speed of sound (SoS) in an ultrasound propagation medium is indispensable for constructing an ultrasound B-mode image, and using an incorrect SoS deteriorates image quality. Moreover, SoS can be used as an indicator for quantifying diseases such as liver steatosis [1]; therefore, accurate SoS estimation is indispensable in quantitative medical ultrasound.

Several studies have been conducted to estimate SoS in propagation media [1–20]. These methods can be categorized into several groups, such as time-delay-based [4–18] and compounding approaches [19, 20]. In time-delay-based approaches, the SoS is estimated from the time-delay distribution of the radiofrequency (RF) waves received by elements in the ultrasound probe. This time-delay distribution is determined by the SoS in the ultrasound propagation medium and the geometric relationship between the target scattering source and known positions of the received elements. One of the time-delay-based approaches directly estimates the SoS from this relationship by detecting the time-delay distribution [4–8]. In other approaches, the time delays among elements are compensated using the preassigned SoS, and the best SoS is determined by optimizing evaluation factors, such as focusing quality [9–12], spatial coherence [11, 13, 14], and coherence factor [15–18].

In these time-delay-based methods, a time-delay distribution is formulated by assuming that the target scatterer

✉ Shohei Mori
mori@tohoku.ac.jp

[1] Graduate School of Engineering, Tohoku University, Sendai, Miyagi 980-8579, Japan

[2] Graduate School of Biomedical Engineering, Tohoku University, Sendai, Miyagi 980-8579, Japan

Published online: 11 March 2023

is an ideal point scatterer. This assumption may hold when the target scatterer is sufficiently thinner than the width of the point spread function (PSF) of the ultrasound. However, the amplitude of the scattered wave from a small scatterer is small and easily affected by the interference of the scattered waves from the surrounding scattering sources. Thus, a large target that exhibits high scattered intensity, such as small vessel walls, is preferable. However, these targets may not be sufficiently smaller than the PSF width, and the assumption of an ideal point scatterer may not hold. In this case, the time-delay distribution must be formulated by considering the target size.

In a previous study [7], we confirmed that the SoS was overestimated when the SoS estimation under the target assumption of the ideal point scatterer was applied to scattered waves from a target with a finite size. Based on the geometric relationship between the target and the elements in the ultrasound probe, a correction method for this overestimated SoS was examined [8]; however, this method assumes that the target size is known. In in vivo measurements, the true target size cannot be measured because the observed size of the target in the ultrasound B-mode image depends on the SoS used for constructing the cross-sectional image. In other words, the true size of the target cannot be known under the condition of an unknown SoS.

In this paper, a method is proposed to estimate the SoS under conditions where the true values of the SoS, target depth, and target size are unknown. To correct the erroneously estimated SoS obtained using the previous method [6], measurable parameters related to the target observed on the B-mode image constructed by the erroneously estimated SoS were used. The proposed method was validated through a water tank experiment using wires with several diameters.

Materials and methods

Assumption of SoS estimation target

In this study, the reception times of the ultrasound waves scattered from a target and received by the elements in the probe were used to estimate the average SoS in the ultrasound propagation medium from the probe surface to the target. As a fundamental study, SoS was assumed to be homogeneous in an ultrasound propagation medium.

To accurately detect the propagation time of the scattered wave from the target, a large target that exhibits high scattered intensity, such as a small blood vessel, is preferable. Thus, SoS estimation method that can be applied to RF signals received from a target of finite size is proposed.

The surface shape of the target inside the transmitted beam width w_{beam} was approximated by a circular form with a curvature radius r as shown in Fig. 1(a) and its expanded version in Fig. 1(b). The shape of the target does not need to be a circle outside the transmitted beam width w_{beam}. The shallowest position of the target surface was assumed to exist exactly below the center (0th element at x_0) of the active elements used for transmitting the beam, as shown in Fig. 1(a). The depth from the probe surface to the shallowest position of the target surface is defined by d, and the lateral position of the 0th element is defined as $x_0 = 0$. Although the focal depth of the transmitted beam was assumed to be set at the target surface, that is, the focal depth was equal to d, as shown in Fig. 1(a), the focused beam was approximated by a plane wave within the beam width w_{beam} around d. The time for transmitting the ultrasonic pulse from the 0th element at x_0 is defined as 0 s.

In the SoS estimation considering the curvature radius r of the target surface, the measurable parameters are the lateral positions of the elements, $\{x_k\}$ (in this paper, $\{\cdot\}$ describes the set of variables), SoS estimate $\widehat{c_{r=0}}$ obtained using the conventional method, assuming an ideal point scatterer ($r = 0$) as a target, and the observed depth $\widehat{d_{\mathrm{B}}}$ and curvature radius $\widehat{r_{\mathrm{B}}}$ of the target surface, that are determined from the B-mode image constructed using the erroneous SoS estimate $\widehat{c_{r=0}}$. The SoS estimate $\widehat{c_{r=0}}$ is not the true value for $r > 0$, and $\widehat{d_{\mathrm{B}}}$ and $\widehat{r_{\mathrm{B}}}$ do not correspond to the true values d and r, respectively.

SoS estimation considering the target size

The proposed SoS estimation method considers the curvature radius r of the target surface, where r is unmeasurable owing to the unknown SoS c. The main concept is to determine the estimation error ratio $\widehat{\rho_r} = \widehat{c_{r=0}}/c$, that is, the ratio of the erroneously estimated SoS $\widehat{c_{r=0}}$ by assuming $r = 0$ to the true SoS c. Here, the bias error is caused by assuming $r \to 0$ when the target has a curvature radius $r > 0$. Once the error ratio $\widehat{\rho_r}$ is determined in the following procedures, the erroneous SoS estimate $\widehat{c_{r=0}}$ can be corrected as

$$\widehat{c_r} = \frac{\widehat{c_{r=0}}}{\widehat{\rho_r}}. \tag{1}$$

The error ratio $\widehat{\rho_r}$ is determined only from the measurable parameters using the following procedures: (I) detection of reception times $\{t(x_k)\}$ for the wavefront of the scattered waves received at elements $\{x_k\}$, (II) SoS $\widehat{c_{r=0}}$ estimation using the conventional method assuming $r = 0$, (III) tentative determination of the depth $\widehat{d_{\mathrm{B}}}$ and curvature radius $\widehat{r_{\mathrm{B}}}$ of the target surface observed on the B-mode image constructed by $\widehat{c_{r=0}}$, and (IV) determination of the estimation

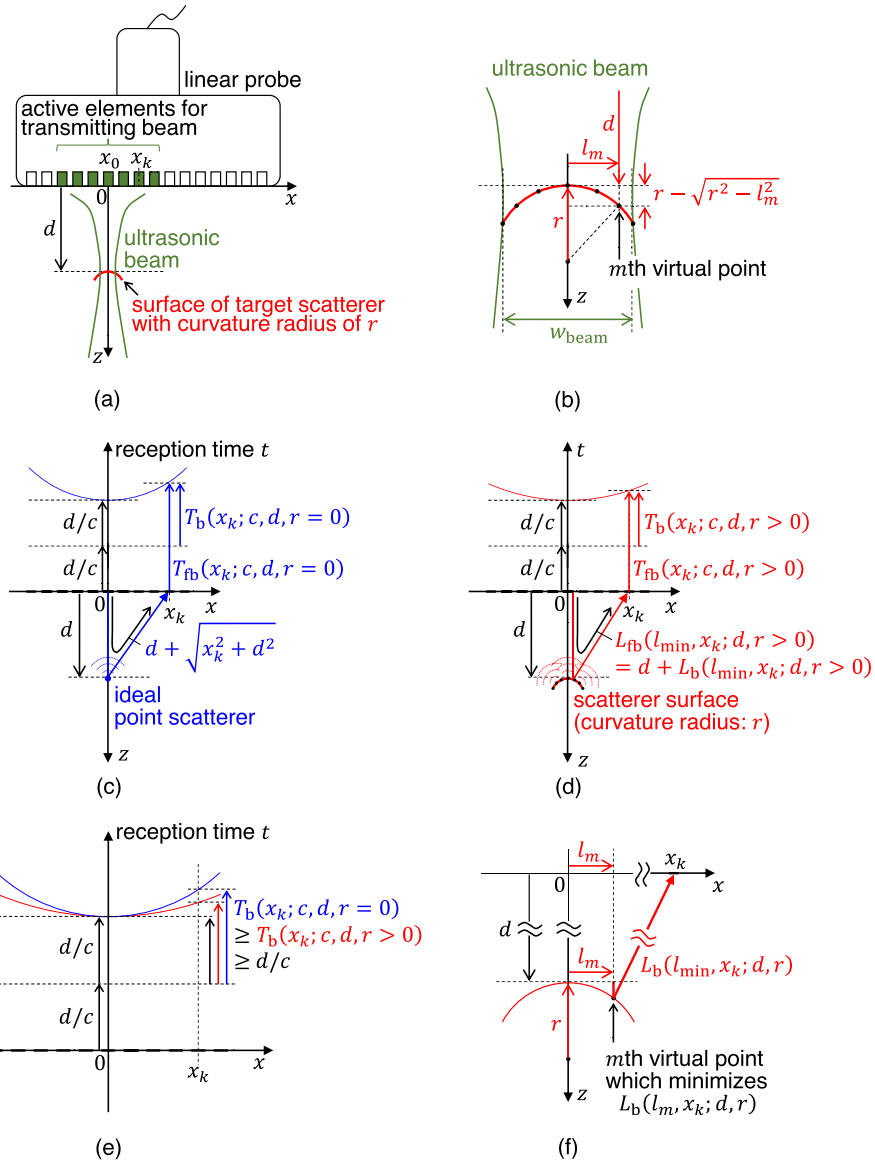

Fig. 1 **a** Schematic of measurement configuration. **b** Definition of target surface within focal region. (**c**, **d**) Propagation paths and reception time distributions of the wavefront of received signals (**c**) from an ideal point scatterer and (**d**) from a target surface having a finite size. **e** Magnitude relationship between $T_{\mathrm{b}}\left(x_k;c,d,r>0\right)$ and $T_{\mathrm{b}}\left(x_k;c,d,r\to 0\right)$. **f** Enlarged view of (**d**) for explaining the definition of $L_{\mathrm{b}}\left(l_{\min},x_k;d,r\right)$

error ratio $\widehat{\rho_r}$ from these measurable parameters to apply Eq. (1). The details of steps (I)–(IV) are described below:

(I) Time detection of the wavefront of the received signal

In the first step, the RF signal of the ultrasound wave scattered from the target is acquired by each element at position x_k, and the reception time $t\left(x_k\right)$ of the wavefront is detected, as shown in Fig. 2. Figure 2(a) shows an example of a B-mode image of the short-axis view of a wire with a diameter $2r = 6$ mm. The received element signals for creating the center received beam, shown by the dashed line in Fig. 2(a), are shown in Fig. 2(b–1), and its expanded version in Fig. 2(b–2). As directly detecting the received time of the wavefront is difficult owing to noise, the time of the wavefront was determined from the pth peak time detected by the peak-detection approach, as in our previous study [7]. In the present study, nylon and silicone wires were used as the targets in the water tank experiment. For nylon wires, the negative peak time $t_{\mathrm{neg}}\left(x_k;p\right)$ was detected. On the contrary, the positive peak time $t_{\mathrm{pos}}\left(x_k;p\right)$ was detected for the silicone wires because the acoustic impedance of the silicone was lower than that of water, and the ultrasound wave was reflected in the opposite phase at the interface between the water and silicone. The reception time $t(x_k)$ of the wavefront is determined as

$$t\left(x_k\right)=\begin{cases} t_{\mathrm{neg}}\left(x_k;p\right)-\frac{p-0.25}{f_0}, & \text{for nylon wires}\\ t_{\mathrm{pos}}\left(x_k;p\right)-\frac{p-0.25}{f_0}, & \text{for silicone wires}\end{cases} \tag{2}$$

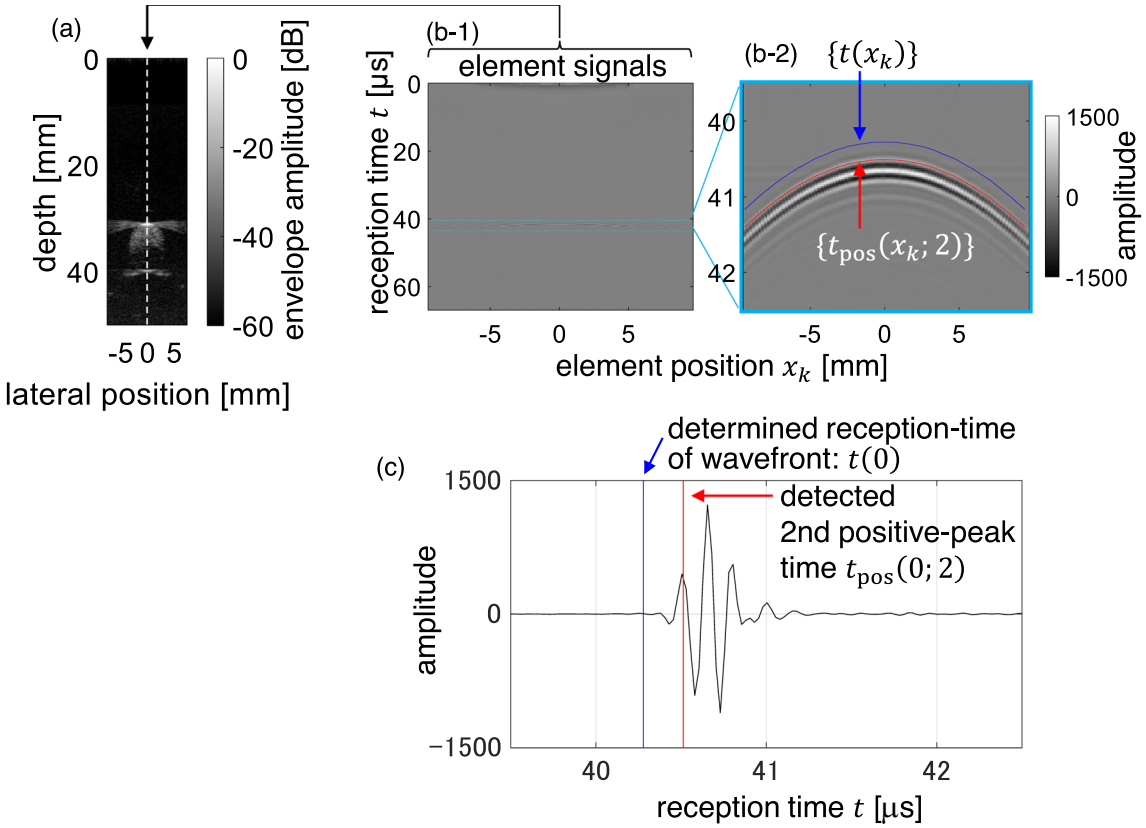

Fig. 2 Schematic for detection of reception time $t(x_k)$ of the wavefront of the received signal from a target. **a** B-mode image of wire with the diameter of $2r = 6$ mm. (**b-1**) Received element signals before beamforming at the ultrasonic beam passing through the center of the wire (white dashed line on (**a**)). (**b-2**) Enlarged view of (**b-1**). **c** Waveform of the element RF signal at $x_k = 0$ in (**b-2**). The detected time of the second positive peak, $t_{\mathrm{pos}}(x_k;2)$, and the determined reception time of the wavefront, $t(x_k)$, are plotted in red and blue, respectively, on (**b-2**) and (**c**)

where f_0 denotes the transmission frequency. The second term represents the compensation of the p th peak time to the time of the wavefront. In this study, the peak number was empirically determined as $p = 2$, which was a condition for stable detection of the peak time. The reception time distribution $\{t(x_k)\}$ is determined from K elements $(k = -(K-1)/2, \cdots, 0, \cdots, (K-1)/2)$, where K is assumed to be an odd number. An example of the detected second peak time distribution $\{t_{\mathrm{pos}}(x_k;2)\}$ and the determined reception time distribution of the wavefront, $\{t(x_k)\}$, are shown in red and blue, respectively, in Fig. 2(b-2). An example of a waveform received by the center element ($x_k = 0$) is shown in Fig. 2(c), with the second peak time $t_{\mathrm{pos}}(0;2)$ (red) and the determined reception time of the wavefront, $t(0)$ (blue). The distribution of time of the wavefront, $\{t(x_k)\}$, is used for SoS estimation using the following procedure.

(II) Conventional SoS estimation, assuming an ideal point scatterer as the target

In the second step, the conventional SoS estimation method [6] is applied to $\{t(x_k)\}$ as follows. As shown in Fig. 1(c), the forward-and-backward propagation time $T_{\mathrm{fb}}(x_k;c,d,r=0)$ of the ultrasound wave transmitted from the probe, scattered by the assumed ideal point scatterer at lateral position $x = 0$ and depth d, and received by the element with position $x = x_k$, is theoretically modeled by

$$T_{\mathrm{fb}}(x_k;c,d,r=0) = \frac{1}{c}\left(d + \sqrt{x_k^2 + d^2}\right). \tag{3}$$

Subsequently, the backward propagation time $T_{\mathrm{b}}(x_k;c,d,r=0)$ is defined by

$$T_{\mathrm{b}}(x_k;c,d,r=0) \equiv T_{\mathrm{fb}}(x_k;c,d,r=0) - \frac{T_{\mathrm{fb}}(0;c,d,r=0)}{2} = \frac{1}{c}\sqrt{x_k^2 + d^2}. \tag{4}$$

Here, $T_{\mathrm{fb}}(0;c,d,r=0) = 2d/c$ corresponds to the measured value $t(0)$, which is the received time of the scattered wave at the 0th element. From Eq. (4),

$$T_{\mathrm{b}}\left(x_k;c,d,r=0\right)^2=\frac{1}{c^2}x_k^2+\frac{d^2}{c^2}. \tag{5}$$

In the actual measurement, the measured propagation time $t\left(x_k\right)$ contains errors; therefore, the quadratic polynomial approximation is applied to the measured values $\left\{\left(t\left(x_k\right)-t(0)/2\right)^2\right\}$ for K elements.

$$\begin{aligned}&\left\{\left(t\left(x_k\right)-\frac{t(0)}{2}\right)^2\right\}\\&\quad\approx a\left\{x_k^2\right\}+b.\ \left(k=-\frac{K-1}{2},\cdots,0,\cdots,\frac{K-1}{2}\right)\end{aligned} \tag{6}$$

By minimizing the mean squared difference between the measured values $\left\{\left(t\left(x_k\right)-t(0)/2\right)^2\right\}$ and their theoretical model $\left\{ax_k^2+b\right\}$, the coefficients a and b of Eq. (6) are determined. Then, SoS $\widehat{c_{r=0}}$ and the target depth $\widehat{d_{r=0}}$ are estimated as follows:

$$\widehat{c_{r=0}}=\sqrt{\frac{1}{\hat{a}}}=\sqrt{\frac{\mathrm{V}_k\left[x_k^2\right]}{\mathrm{COV}_k\left[x_k^2,\left(t\left(x_k\right)-\frac{t(0)}{2}\right)^2\right]}},\ \ [\mathrm{m/s}] \tag{7}$$

$$\widehat{d_{r=0}}=\sqrt{\frac{\hat{b}}{\hat{a}}}=\sqrt{\frac{1}{\hat{a}}\mathrm{E}_k\left[\left(t\left(x_k\right)-\frac{t(0)}{2}\right)^2\right]-\mathrm{E}_k\left[x_k^2\right]},\ \ [\mathrm{m}] \tag{8}$$

where $\mathrm{E}_k[\cdot]$, $\mathrm{V}_k[\cdot]$, and $\mathrm{COV}_k[\cdot,\cdot]$ are the average, variance, and covariance for k, respectively. Detailed derivations of Eqs. (7) and (8) are presented in Appendix A (see the electronic supplementary material). When the target is an ideal point scatterer ($r=0$) and the measured propagation time has no errors, the measured values $\left\{\left(t\left(x_k\right)-t(0)/2\right)^2\right\}$ correspond to $\left\{T_{\mathrm{b}}\left(x_k;c,d,r=0\right)^2\right\}$; therefore, $\widehat{c_{r=0}}$ and $\widehat{d_{r=0}}$ correspond to the true values c and d, respectively.

However, when the surface of the target has a curvature radius r, as shown in Fig. 1(d), the forward-and-backward propagation time distribution $\left\{T_{\mathrm{fb}}\left(x_k;c,d,r>0\right)\right\}$ is affected by r as follows. Based on our previous study [7], several virtual points are set on the target surface (curvature radius r), as shown in Figs. 1(a, b). By approximating the focused beam by a plane wave within the narrow ultrasonic beam and around the focal depth, the propagation distance from the element exactly above the m th virtual point on the target surface to the m th virtual point is $d+r-\sqrt{r^2-l_m^2}$, as shown in Figs. 1(b, d), where l_m is the lateral position of the m th virtual point from the centerline ($x=0$) passing through the 0th element. The propagation distance from the m th virtual point to the k th element at x_k is $\sqrt{\left(x_k-l_m\right)^2+\left(d+r-\sqrt{r^2-l_m^2}\right)^2}$, as shown in Figs. 1(b, d). By taking the sum of these two distances, the forward-and-backward propagation distance $L_{\mathrm{fb}}\left(l_m,x_k;d,r\right)$ from the element exactly above the m th virtual point to k th element via m th virtual point is

$$\begin{aligned}L_{\mathrm{fb}}\left(l_m,x_k;d,r\right)&=d+r-\sqrt{r^2-l_m^2}\\&\quad+\sqrt{\left(x_k-l_m\right)^2+\left(d+r-\sqrt{r^2-l_m^2}\right)^2}.\end{aligned} \tag{9}$$

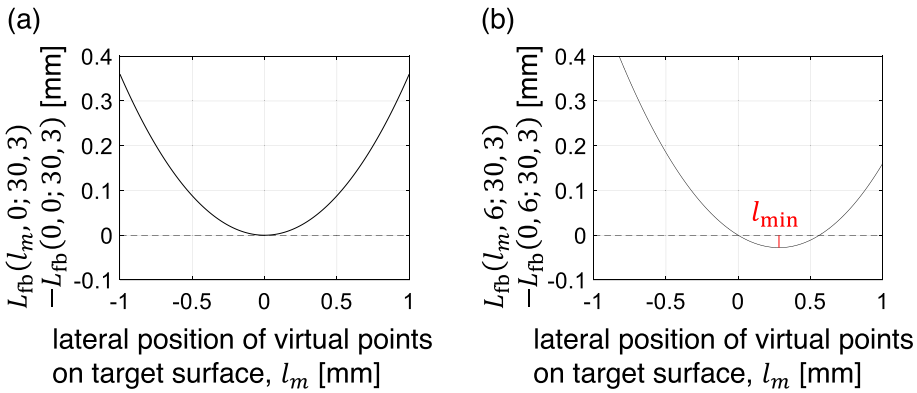

Fig. 3 Examples of $L_{\mathrm{fb}}\left(l_m,x_k;d,r\right)-L_{\mathrm{fb}}\left(0,x_k;d,r\right)$ obtained for $d=30$ mm and $r=3$ mm. The received element positions are **a** $x_k=0$ and **b** $x_k=6$ mm

When the m th virtual point is on the centerline ($l_m = 0$), the distance $L_{\mathrm{fb}}(0, x_k; d, r)$ is given by

$$L_{\mathrm{fb}}(0, x_k; d, r) = d + \sqrt{x_k^2 + d^2}, \tag{10}$$

which equals the forward-and-backward propagation distance when the target is an ideal point scatterer ($r \to 0$), as shown in Fig. 1(c) and modeled in Eq. (3).

Figure 3 shows examples of $L_{\mathrm{fb}}(l_m, x_k; d, r) - L_{\mathrm{fb}}(0, x_k; d, r)$ obtained for target conditions of $d = 30$ mm and $r = 3$ mm for $x_k = 0$ and $x_k = 6$ mm. When the received element is on the centerline ($x_k = 0$), as shown in Fig. 3(a), $L_{\mathrm{fb}}(l_m, 0; d, r)$ equals its minimum $L_{\mathrm{fb}}(0, x_k; d, r)$ for $l_m = 0$ and is longer than $L_{\mathrm{fb}}(0, x_k; d, r)$ for $l_m \neq 0$. However, when the received element is not on the centerline ($x_k \neq 0$), as shown in Fig. 3(b), there are propagation paths shorter than the distance $L_{\mathrm{fb}}(0, x_k; d, r)$. Thus, the following relationship holds.

$$L_{\mathrm{fb}}(l_{\min}, x_k; d, r) \le L_{\mathrm{fb}}(0, x_k; d, r) = d + \sqrt{x_k^2 + d^2}, \tag{11}$$

where $L_{\mathrm{fb}}(l_{\min}, x_k; d, r)$ is the minimum of $\{L_{\mathrm{fb}}(l_m, x_k; d, r)\}$ for l_m within the transmitted beam width w_{beam}, and is given by

$$L_{\mathrm{fb}}(l_{\min}, x_k; d, r) = \min_{l_m} L_{\mathrm{fb}}(l_m, x_k; d, r). \quad |l_m| \le \min\left(r, \frac{w_{\mathrm{beam}}}{2}\right) \tag{12}$$

In our previous study [7], we confirmed that the received time of the wavefront of the interfered waves from the virtual points on the target surface can be approximated by the received time of the wavefront of the "first arrival wave" among the virtual points $\{m\}$ on the target surface. Using Eq. (12), the forward-and-backward propagation time $T_{\mathrm{fb}}(x_k; c, d, r)$ of this "first arrival wave" is given by

$$T_{\mathrm{fb}}(x_k; c, d, r) = \frac{1}{c} L_{\mathrm{fb}}(l_{\min}, x_k; d, r). \quad (r \ge 0) \tag{13}$$

When the target is an ideal point scatterer ($r = 0$), Eq. (13) is equivalent to that in Eq. (3).

When the target has a size ($r > 0$), the backward propagation time $T_{\mathrm{b}}(x_k; c, d, r)$ defined by Eq. (4) is given by

$$\begin{aligned} T_{\mathrm{b}}(x_k; c, d, r) &= T_{\mathrm{fb}}(x_k; c, d, r) - \frac{d}{c} \\ &= \frac{1}{c} L_{\mathrm{fb}}(l_{\min}, x_k; d, r) - \frac{d}{c} \\ &= \frac{1}{c} L_{\mathrm{b}}(l_{\min}, x_k; d, r), \end{aligned} \tag{14}$$

where $L_{\mathrm{b}}(l_{\min}, x_k; d, r)$ is the backward propagation distance defined in Fig. 1(f), and is given by

$$L_{\mathrm{b}}(l_{\min}, x_k; d, r) \equiv L_{\mathrm{fb}}(l_{\min}, x_k; d, r) - d. \tag{15}$$

By substituting $T_{\mathrm{b}}(x_k; c, d, r)$ of Eq. (14) for $T_{\mathrm{b}}(x_k; c, d, r = 0)$ of Eq. (5) or its measured value, $t(x_k) - t(0)/2$ of Eq. (7), the SoS estimate $\widehat{c_{r=0}}$ of Eq. (7) by assuming that $r = 0$ is given by

$$\widehat{c_{r=0}} = \sqrt{\frac{\mathrm{V}_k\left[x_k^2\right]}{\mathrm{COV}_k\left[x_k^2, T_{\mathrm{b}}(x_k; c, d, r)^2\right]}}, \tag{16}$$

which is the theoretical erroneous estimate under the noise-free condition, whose bias error is caused by assuming $r \to 0$ despite the target having a curvature radius $r > 0$, *i.e.*, the error is caused by the fact that $T_b(x_k \neq 0; c, d, r > 0)$ in Eq. (14) is shorter than $T_{\mathrm{b}}(x_k \neq 0; c, d, r \to 0)$, as shown in Fig. 3(b). From Eq. (16), the theoretical estimation error ratio ρ_r in Eq. (1) can be expressed as follows:

$$\begin{aligned} \rho_r &= \frac{\widehat{c_{r=0}}}{c} \\ &= \frac{1}{c}\sqrt{\frac{\mathrm{V}_k\left[x_k^2\right]}{\mathrm{COV}_k\left[x_k^2, T_{\mathrm{b}}(x_k; c, d, r)^2\right]}} = \sqrt{\frac{\mathrm{V}_k\left[x_k^2\right]}{\mathrm{COV}_k\left[x_k^2, c^2 T_{\mathrm{b}}(x_k; c, d, r)^2\right]}} \\ &= \sqrt{\frac{\mathrm{V}_k\left[x_k^2\right]}{\mathrm{COV}_k\left[x_k^2, L_{\mathrm{b}}(l_{\min}, x_k; d, r)^2\right]}}, \end{aligned} \tag{17}$$

where the last equation is obtained from Eq. (14). Equation (17) shows that the estimation error ratio ρ_r depends only on the geometric variables of x_k, d, and r, and does not depend on the true SoS value c.

As shown by Eqs. (6) and (7), the SoS estimate $\widehat{c_{r=0}}$ is determined by $1/\sqrt{a}$ of the squared propagation time distribution $\left\{\left(t(x_k) - t(0)/2\right)^2\right\}$. Because $2a$ is the curvature of $\left\{T_{\mathrm{b}}(x_k; c, d, r)^2\right\}$ around $x_k = 0$, the relationship between the curvatures of $\left\{T_{\mathrm{b}}(x_k; c, d, r > 0)^2\right\}$ and $\left\{T_{\mathrm{b}}(x_k; c, d, r \to 0)^2\right\}$, which correspond to $\left\{\left(t(x_k) - t(0)/2\right)^2\right\}$ when $r > 0$ and $r \to 0$, respectively, was evaluated to clarify the relationship between $\widehat{c_{r=0}}$ and c.

First, by substituting $L_{\mathrm{fb}}(l_{\min}, x_k; d, r)$ in Eq. (11) into Eq. (15) and the resultant $L_{\mathrm{b}}(l_{\min}, x_k; d, r)$ into Eq. (14),

$$T_{\mathrm{b}}(x_k; c, d, r) \le \frac{1}{c}\sqrt{x_k^2 + d} = T_{\mathrm{b}}(x_k; c, d, r \to 0). \tag{18}$$

Second, as shown in Fig. 1(d), the backward propagation time $T_{\mathrm{b}}(x_k; c, d, r)$ is minimized at $x_k = 0$ as

$$\min_{x_k} T_b\left(x_k;c,d,r\right) = T_b(0;c,d,r) = \frac{d}{c}. \tag{19}$$

That is,

$$\begin{aligned} T_b(0;\,c,d,r) &= \frac{d}{c} \le T_b\left(x_k;\,c,d,r\right) \\ &\le \frac{1}{c}\sqrt{x_k^2+d} = T_b\left(x_k;\,c,d,r\to 0\right). \end{aligned} \tag{20}$$

This relationship is illustrated in Fig. 1(e). Thus, the factor of curvature, a, of the squared backward propagation time distribution $\left\{T_b\left(x_k;c,d,r>0\right)^2\right\}$ is smaller than that of $\left\{T_b\left(x_k;c,d,r\to 0\right)^2\right\}$, and SoS $\widehat{c_{r=0}}$ is always overestimated for $r>0$ as

$$\rho_r = \frac{\widehat{c_{r=0}}}{c} > 1, \quad (r>0) \tag{21}$$

which was experimentally confirmed in our previous study [7].

As shown in Eq. (12), the minimum propagation distance $L_{fb}\left(l_{min},x_k;d,r\right)$ changes with the transmitted beam width w_{beam}; therefore, the estimation error ratio ρ_r also changes with w_{beam}. By narrowing the transmitted beam width w_{beam}, $L_{fb}\left(l_{min},x_k;d,r\right)$ approaches the condition of an ideal point scatterer, $L_{fb}\left(l_{min},x_k;d,r=0\right)$, and the estimation error ratio ρ_r decreases. However, by theoretically evaluating the relationship between the transmitted beam width w_{beam} and SoS estimation error ratio ρ_r based on Eqs. (12–17), a positive error larger than 10 m/s is caused for target radius $r \ge 1$ mm even if the transmitted beam width w_{beam} is narrowed to 0.2 mm (wavelength for transmitted frequency: 7.5 MHz; SoS: 1,500 m/s). In practice, the transmitted beam width w_{beam} generally becomes larger than the wavelength; therefore, SoS correction by the following method is essential for estimating the true SoS irrespective of the target size.

(III) Measurable parameters related to the target surface observed in the B-mode image

To correct the erroneously estimated SoS $\widehat{c_{r=0}}$ from the measurable parameters $\widehat{d_B}$ and $\widehat{r_B}$ on the B-mode image, the relationships between the measurable parameters $(\widehat{d_B},\widehat{r_B})$ and the unmeasurable true values (d,r) were clarified as follows:

Figures 4(a, b) illustrates examples of B-mode images constructed using the true SoS c and erroneous estimate $\widehat{c_{r=0}}$ $(\widehat{c_{r=0}} > c)$, respectively. The B-mode image in Fig. 4(a) cannot be constructed owing to the unknown true SoS c, whereas the B-mode image in Fig. 4(b) can be constructed using the erroneous estimate $\widehat{c_{r=0}}$.

Let $z_B\left(x_{beam};c\right)$ be the depth position of the target surface in the B-mode image constructed using the true SoS c, as shown in Fig. 4(a). $z_B\left(x_{beam};c\right)$ corresponds to the depth along the ultrasound-focused beam at x_{beam} and is described by

$$z_B\left(x_{beam};c\right) = d + r - \sqrt{r^2 - x_{beam}^2} = \frac{c\cdot t\left(x_{beam}\right)}{2}, \tag{22}$$

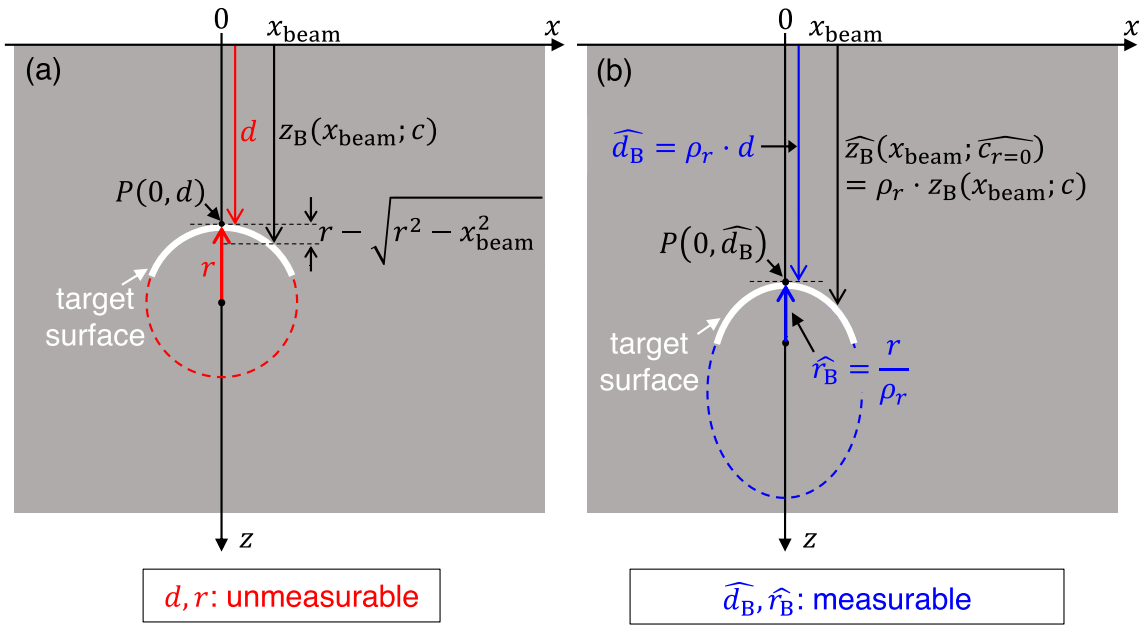

Fig. 4 Schematic of measurable and unmeasurable parameters on the B-mode image. **a** B-mode image constructed by true SoS c, which cannot be obtained by in vivo measurement. **b** B-mode image constructed by erroneously estimated SoS $\widehat{c_{r=0}}$, which can be obtained without the knowledge of the true SoS c. $\widehat{r_B}$ shows the curvature radius around point $P\left(0,\widehat{d_B}\right)$

where $t\left(x_{\text{beam}}\right)$ is the received time of the scattered wave from the target surface with lateral position x_{beam}. Depth $z_{\text{B}}(0;c)$ at $x_{\text{beam}} = 0$ corresponds to the shallowest depth d of the target surface as follows:

$$z_{\text{B}}(0;c) = d. \tag{23}$$

However, when the B-mode image is constructed using the erroneously estimated SoS $\widehat{c_{r=0}}$, the depth position $\hat{z}_{\text{B}}(x_{\text{beam}};\widehat{c_{r=0}})$ of the target surface observed in Fig. 4(b) can be described by

$$\begin{aligned}\hat{z}_{\text{B}}\left(x_{\text{beam}};\widehat{c_{r=0}}\right) &= \frac{\widehat{c_{r=0}} \cdot t\left(x_{\text{beam}}\right)}{2} \\ &= \frac{\widehat{c_{r=0}}}{c} \cdot \frac{c \cdot t\left(x_{\text{beam}}\right)}{2} = \rho_r \cdot z_{\text{B}}\left(x_{\text{beam}};c\right),\end{aligned} \tag{24}$$

where the last equation is obtained using Eqs. (21) and (22), respectively. Thus, the measurable depth of the target surface, $\hat{z}_{\text{B}}\left(x_{\text{beam}};\widehat{c_{r=0}}\right)$, is given as a multiple of the true depth $z_{\text{B}}\left(x_{\text{beam}};c\right)$ by a factor of $\rho_r \geq 1$, as shown in Fig. 4(b). From Eq. (24), the shallowest depth of the target surface, $\widehat{d_{\text{B}}}$, observed in the B-mode image constructed using $\widehat{c_{r=0}}$ is determined by

$$\begin{aligned}\widehat{d_{\text{B}}} &= \hat{z}_{\text{B}}\left(0;\widehat{c_{r=0}}\right) \\ &= \rho_r \cdot z_{\text{B}}(0;c) = \rho_r \cdot d,\end{aligned} \tag{25}$$

where the last equation is obtained from Eq. (23).

Next, the shape of the target surface observed in the B-mode image was considered as follows. The shape of the target surface, shown in Fig. 4(a), is described by Eq. (22) as

$$x_{\text{beam}}^2 + \left[z_{\text{B}}\left(x_{\text{beam}};c\right) - (d+r)\right]^2 = r^2, \tag{26}$$

which is a circular equation with radius r. In contrast, the shape of the target surface in Fig. 4(b) is described by substituting $z_{\text{B}}\left(x_{\text{beam}};c\right)$ in Eq. (22) into Eq. (24),

$$\left(\frac{x_{\text{beam}}}{r}\right)^2 + \left(\frac{\hat{z}_{\text{B}}\left(x_{\text{beam}};\widehat{c_{r=0}}\right) - \rho_r(d+r)}{\rho_r \cdot r}\right)^2 = 1. \tag{27}$$

This shows that the target of a circle with radius r in Fig. 4(a) and Eq. (26) is observed as an ellipse with minor radius r and major radius $\rho_r \cdot r \geq r$ in Fig. 4(b).

In the proposed SoS estimation method, only the curvature radius r around the shallowest depth d of the target surface within the transmitted beam width w_{beam} was considered, as shown in Fig. 1(a). Therefore, the relationship between the measurable curvature radius $\hat{r}_{\text{B}}$ around point $P\left(0, \widehat{d_{\text{B}}}\right)$ in Fig. 4(b) and the true curvature radius r in Fig. 4(a) is formulated as follows:

From the curvature formula, the curvature radius $\hat{r}_{\text{B}}$ around $P\left(0, \widehat{d_{\text{B}}}\right)$ is given by

$$\begin{aligned}\hat{r}_{\text{B}} &= \frac{\left[1+\left(\left.\frac{d\,\hat{z}_{\text{B}}\left(x_{\text{beam}};\widehat{c_{r=0}}\right)}{d\,x_{\text{beam}}}\right|_{x_{\text{beam}}=0}\right)^2\right]^{\frac{3}{2}}}{\left|\left.\frac{d^2\,\hat{z}_{\text{B}}\left(x_{\text{beam}};\widehat{c_{r=0}}\right)}{d\,x_{\text{beam}}^2}\right|_{x_{\text{beam}}=0}\right|} \\ &= \frac{1}{\frac{\rho_r}{r}} = \frac{r}{\rho_r},\end{aligned} \tag{28}$$

where the second equation is obtained by substituting $z_{\text{B}}\left(x_{\text{beam}};c\right)$ in Eq. (22) into Eq. (24), and substituting the resultant $\hat{z}_{\text{B}}\left(x_{\text{beam}};\widehat{c_{r=0}}\right)$ into the first equation in Eq. (28). The derivation of the first equation in Eq. (28) is described in Appendix B (see the electronic supplementary material). Thus, the curvature radius $\hat{r}_{\text{B}}$ around point $P\left(0, \widehat{d_{\text{B}}}\right)$ in

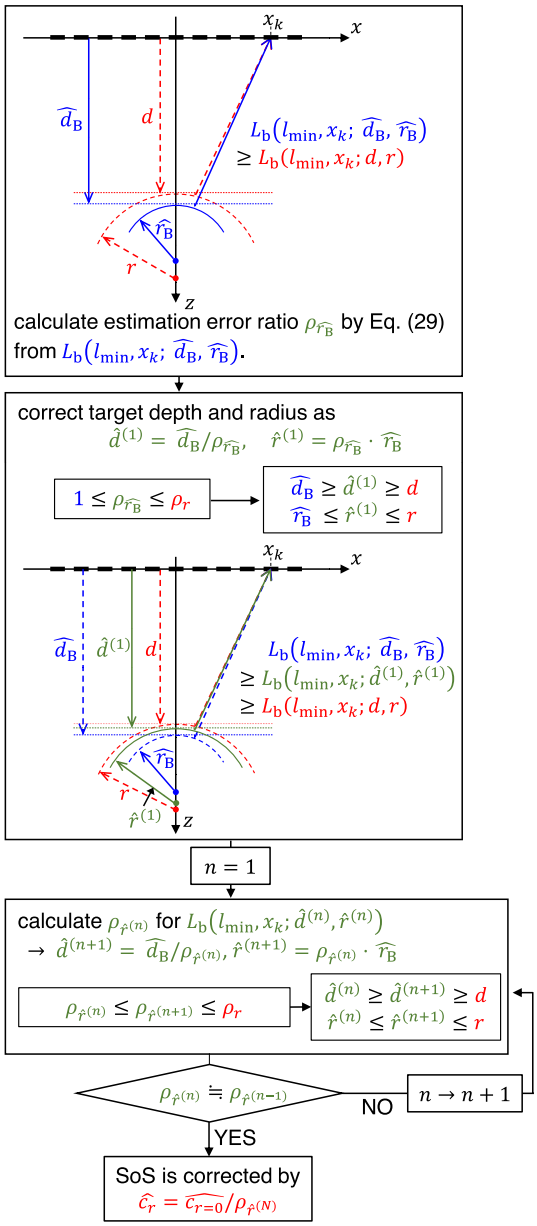

Fig. 5 Procedure for the proposed SoS correction method

Fig. 4(b) becomes smaller than the true radius r with a factor of $(1/\rho_r) \leq 1$. This relationship can also be derived from the property of the ellipse, that is, the curvature radius of the ellipse around the position on the major axis, $P\left(0, \widehat{d_{\mathrm{B}}}\right)$ in Fig. 4(b), is given by the ratio of the squared minor radius to the major radius, $\widehat{r_{\mathrm{B}}} = r^2/(\rho_r \cdot r) = r/\rho_r$.

Thus, we can measure $\widehat{d_{\mathrm{B}}} = \rho_r \cdot d$ and $\widehat{r_{\mathrm{B}}} = r/\rho_r$ from the B-mode image constructed by the erroneously estimated SoS $\widehat{c_{r=0}}$; however, we still cannot determine the true values of d, r, and ρ_r. Based on these relationships, the erroneous estimate $\widehat{c_{r=0}}$ is corrected using $\widehat{d_{\mathrm{B}}}$ and $\widehat{r_{\mathrm{B}}}$ as follows:

(IV) Determination of the estimation error ratio ρ_r from measurable parameters $(\widehat{d_{\mathrm{B}}}, \widehat{r_{\mathrm{B}}})$

The actual target depth d and curvature radius r are estimated from the measurable parameters $\widehat{d_{\mathrm{B}}}$ and $\widehat{r_{\mathrm{B}}}$ using the relationship between the measurable parameters $(\widehat{d_{\mathrm{B}}}, \widehat{r_{\mathrm{B}}})$ and the true values (d, r) determined by Eqs. (25) and (28). Figure 5 shows the proposed procedure for iterations for correction.

First, by substituting $\widehat{d_{\mathrm{B}}}$ and $\widehat{r_{\mathrm{B}}}$ for d and r in Eq. (15), the backward propagation distance distribution $\left\{L_{\mathrm{b}}\left(l_{\min}, x_k; \widehat{d_{\mathrm{B}}}, \widehat{r_{\mathrm{B}}}\right)\right\}$ is obtained. The error ratio $\rho_{\widehat{r_{\mathrm{B}}}}$ is then obtained by substituting $L_{\mathrm{b}}\left(l_{\min}, x_k; \widehat{d_{\mathrm{B}}}, \widehat{r_{\mathrm{B}}}\right)$ for $L_{\mathrm{b}}\left(l_{\min}, x_k; d, r\right)$ in Eq. (17),

$$\rho_{\widehat{r_{\mathrm{B}}}} = \sqrt{\frac{\mathrm{V}_k\left[x_k^2\right]}{\mathrm{COV}_k\left[x_k^2, L_{\mathrm{b}}\left(l_{\min}, x_k; \widehat{d_{\mathrm{B}}}, \widehat{r_{\mathrm{B}}}\right)^2\right]}}, \tag{29}$$

where the bias error is caused by assuming $\widehat{r_{\mathrm{B}}} \to 0$ although the target has a curvature radius $\widehat{r_{\mathrm{B}}} > 0$.

The relationship between $\rho_{\widehat{r_{\mathrm{B}}}}$ and the theoretical estimation error ratio ρ_r obtained using Eq. (17) under true target conditions (d, r) was evaluated as follows. By dividing $\rho_{\widehat{r_{\mathrm{B}}}}$ in Eq. (29) using ρ_r in Eq. (17), and substituting $\widehat{d_{\mathrm{B}}}$ in Eq. (25) and $\widehat{r_{\mathrm{B}}}$ in Eq. (28) into Eq. (29),

$$\begin{aligned}\frac{\rho_{\widehat{r_{\mathrm{B}}}}}{\rho_r} &= \sqrt{\frac{\mathrm{COV}_k\left[x_k^2, L_{\mathrm{b}}\left(l_{\min}, x_k; d, r\right)^2\right]}{\mathrm{COV}_k\left[x_k^2, L_{\mathrm{b}}\left(l_{\min}, x_k; \widehat{d_{\mathrm{B}}}, \widehat{r_{\mathrm{B}}}\right)^2\right]}} \\ &= \sqrt{\frac{\mathrm{COV}_k\left[x_k^2, L_{\mathrm{b}}\left(l_{\min}, x_k; d, r\right)^2\right]}{\mathrm{COV}_k\left[x_k^2, L_{\mathrm{b}}\left(l_{\min}, x_k; \rho_r \cdot d, \frac{r}{\rho_r}\right)^2\right]}}.\end{aligned} \tag{30}$$

To evaluate $\rho_{\widehat{r_{\mathrm{B}}}}/\rho_r$ of Eq. (30), $\mathrm{COV}_k\left[x_k^2, L_{\mathrm{b}}\left(l_{\min}, x_k; d, r\right)^2\right]$ and $\mathrm{COV}_k\left[x_k^2, L_{\mathrm{b}}\left(l_{\min}, x_k; \rho_r \cdot d, r/\rho_r\right)^2\right]$ were simulated in advance for each set of the assumed parameter values $(\{x_k\}, d, r)$, where d is changed from 10 to 60 mm at 0.1-mm intervals, r is changed from 0 to 5 mm at 0.02-mm intervals, and $\{x_k\}$ is set from -9.6 to 9.6 mm at 0.2-mm intervals. Here, the set values $(\{x_k\}, d, r)$ were substituted into Eqs. (9), (12), and (15) to obtain $\{L_{\mathrm{b}}(l_{\min}, x_k; d, r)\}$, and the resultant $\{L_{\mathrm{b}}(l_{\min}, x_k; d, r)\}$ were substituted into Eq. (17) to obtain ρ_r. Subsequently, $\{L_{\mathrm{b}}(l_{\min}, x_k; \rho_r \cdot d, r/\rho_r)\}$ were obtained by substituting $(\{x_k\}, \rho_r \cdot d, r/\rho_r)$ into Eqs. (9), (12), and (15). Finally, $\mathrm{COV}_k\left[x_k^2, L_{\mathrm{b}}\left(l_{\min}, x_k; d, r\right)^2\right]$ and $\mathrm{COV}_k\left[x_k^2, L_{\mathrm{b}}\left(l_{\min}, x_k; \rho_r \cdot d, r/\rho_r\right)^2\right]$ were obtained by calculating the covariance of $\{x_k\}$ and $\{L_{\mathrm{b}}(l_{\min}, x_k; d, r)\}$, or the covariance of $\{x_k\}$ and $\{L_{\mathrm{b}}(l_{\min}, x_k; \rho_r \cdot d, r/\rho_r)\}$, respectively. The results obtained for all the parameter values $\{(\{x_k\}, d, r)\}$ are shown in Fig. 6(a). As shown in Fig. 6(a), $\mathrm{COV}_k\left[x_k^2, L_{\mathrm{b}}\left(l_{\min}, x_k; \rho_r \cdot d, r/\rho_r\right)^2\right]$ is always equal to or larger than $\mathrm{COV}_k\left[x_k^2, L_{\mathrm{b}}\left(l_{\min}, x_k; d, r\right)^2\right]$, that is, ρ_r is always equal to or larger than $\rho_{\widehat{r_{\mathrm{B}}}}$. Because the error ratio is equal to 1 for $r = 0$ and greater than 1 for $r > 0$, as confirmed in Eq. (21), the following relationship holds:

$$1 \leq \rho_{\widehat{r_{\mathrm{B}}}} \leq \rho_r. \tag{31}$$

Thus, from Eq. (31), the depth $\widehat{d}^{(1)} = \widehat{d_{\mathrm{B}}}/\rho_{\widehat{r_{\mathrm{B}}}}$ and curvature radius $\widehat{r}^{(1)} = \rho_{\widehat{r_{\mathrm{B}}}} \cdot \widehat{r_{\mathrm{B}}}$ both corrected by $\rho_{\widehat{r_{\mathrm{B}}}}$ approach the true values d and r, respectively, as follows:

$$\widehat{d_{\mathrm{B}}} \geq \widehat{d}^{(1)} = \frac{\widehat{d_{\mathrm{B}}}}{\rho_{\widehat{r_{\mathrm{B}}}}} \geq \frac{\widehat{d_{\mathrm{B}}}}{\rho_r} = d, \tag{32}$$

$$\widehat{r_{\mathrm{B}}} \leq \widehat{r}^{(1)} = \rho_{\widehat{r_{\mathrm{B}}}} \cdot \widehat{r_{\mathrm{B}}} \leq \rho_r \cdot \widehat{r_{\mathrm{B}}} = r. \tag{33}$$

Using a similar procedure, $\rho_{\widehat{r}^{(n)}}$ $(\rho_{\widehat{r}^{(0)}} \equiv \rho_{\widehat{r_{\mathrm{B}}}})$ is iteratively obtained for the backward propagation distance distribution $\left\{L_{\mathrm{b}}\left(l_{\min}, x_k; \hat{d}^{(n)}, \hat{r}^{(n)}\right)\right\}$, using Eq. (17) as

$$\rho_{\widehat{r}^{(n)}} = \sqrt{\frac{\mathrm{V}_k\left[x_k^2\right]}{\mathrm{COV}_k\left[x_k^2, L_{\mathrm{b}}\left(l_{\min}, x_k; \hat{d}^{(n)}, \hat{r}^{(n)}\right)^2\right]}}. \tag{34}$$

Similarly with Eq. (31),

$$\rho_{\widehat{r}^{(n)}} \leq \rho_{\widehat{r}^{(n+1)}} \leq \rho_r. \quad (n \geq 0) \tag{35}$$

Then, from the relationship in Eq. (35), $\widehat{d}^{(n+1)} = \widehat{d_{\mathrm{B}}}/\rho_{\widehat{r}^{(n)}}$ and $\widehat{r}^{(n+1)} = \rho_{\widehat{r}^{(n)}} \cdot \widehat{r_{\mathrm{B}}}$ both corrected by $\rho_{\widehat{r}^{(n)}}$ approach their true values as follows:

$$\widehat{d}^{(n)} \geq \widehat{d}^{(n+1)} = \frac{\widehat{d_{\mathrm{B}}}}{\rho_{\widehat{r}^{(n)}}} \geq d, \tag{36}$$

$$\widehat{r}^{(n)} \leq \widehat{r}^{(n+1)} = \rho_{\widehat{r}^{(n)}} \cdot \widehat{r_{\mathrm{B}}} \leq r. \tag{37}$$

Therefore, by iterative correction, the measured target depth $\widehat{d_{\mathrm{B}}}$ and curvature radius $\widehat{r_{\mathrm{B}}}$ converge to the true values d and r, respectively.

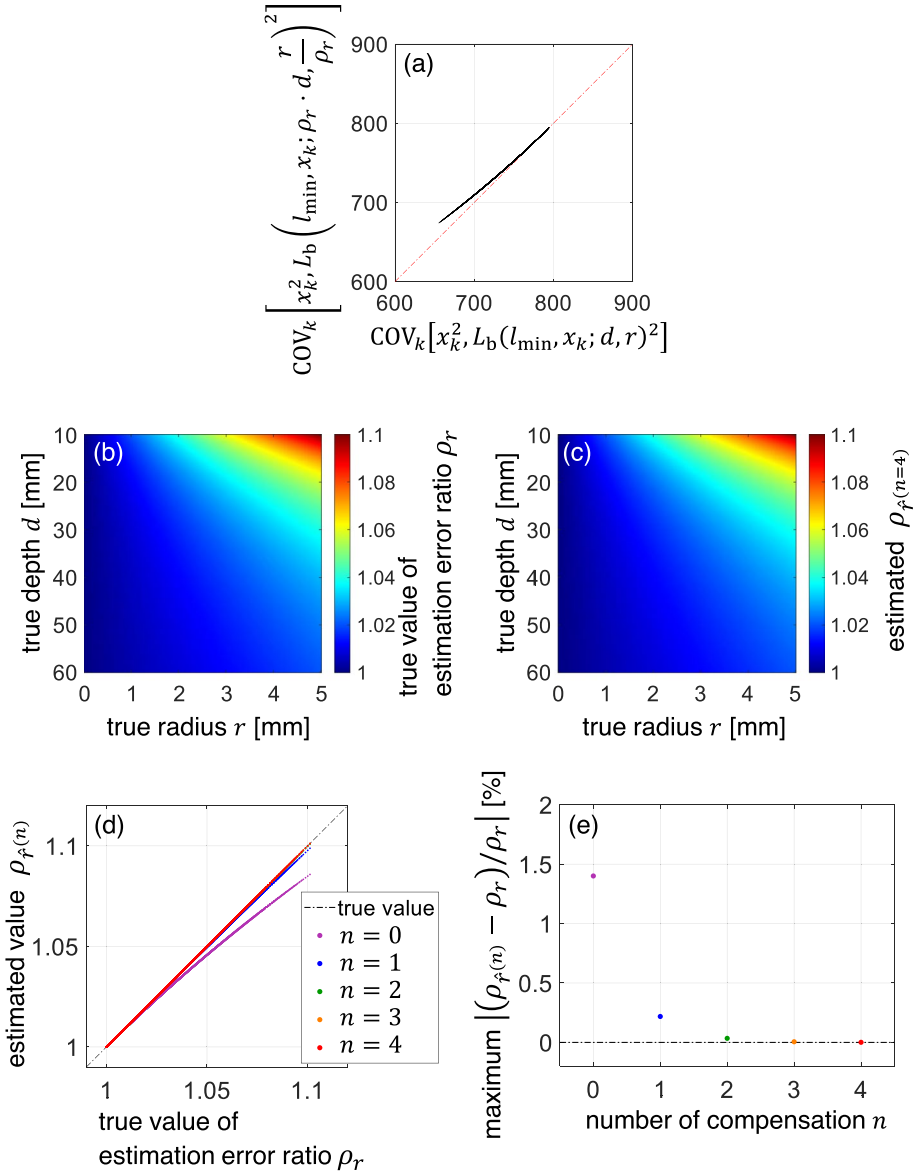

Fig. 6 Theoretical validation for the proposed SoS correction method. **a** Theoretical relationship between $\mathrm{COV}_k\left[x_k^2, L_b\left(l_{\min}, x_k; d, r\right)^2\right]$ and $\mathrm{COV}_k\left[x_k^2, L_b\left(l_{\min}, x_k; \rho_r \cdot d, r/\rho_r\right)^2\right]$ obtained for each set of the parameters (d, r), which shows the relationship of true estimation error ratio ρ_r obtained by Eq. (17) and $\rho_{\hat{r}_B}$ obtained by Eq. (29). **b** True values of estimation error ratio ρ_r obtained by Eq. (17). **c** Estimation error ratio $\rho_{\hat{r}^{(n=4)}}$ determined by four iterations using Eq. (34). **d** Relationship between the true estimation error ratio ρ_r and estimated $\rho_{\hat{r}^{(n)}}$. **e** Normalized maximum difference $\left|\left(\rho_{\hat{r}^{(n)}} - \rho_r\right)/\rho_r\right|$

Thus, based on the relationship between the measurable parameters $(\widehat{d_B}, \widehat{r_B})$ and true values (d, r) determined using Eqs. (25) and (28), the error ratio $\rho_{\hat{r}^{(0)}} \equiv \rho_{\widehat{r_B}}$ is iteratively corrected to the true value ρ_r based on Eq. (35). Finally, the erroneously estimated SoS $\widehat{c_{r=0}}$ is corrected as follows:

$$\widehat{c_r} = \frac{\widehat{c_{r=0}}}{\rho_{\hat{r}^{(N)}}}, \tag{38}$$

where N denotes the total number of iterations.

Figure 6(b) shows the theoretical estimation error ratio ρ_r for each set of parameters (d, r) obtained using Eq. (17). Figure 6(c) shows $\rho_{\hat{r}^{(4)}}$ obtained using Eq. (34) with four iterations. $\rho_{\hat{r}^{(4)}}$ in Fig. 6(c) corresponds well to the true value ρ_r in Fig. 6(b). Figure 6(d) shows the relationship between ρ_r and $\rho_{\hat{r}^{(n)}}$ for each parameter set (d, r), and Fig. 6(e) shows the normalized maximum difference $\left|\left(\rho_{\hat{r}^{(n)}} - \rho_r\right)/\rho_r\right|$. Figures 6(d, e) show that the estimated $\rho_{\hat{r}^{(n)}}$ converged to the true value ρ_r by iterative correction. The normalized maximum differences $\left|\left(\rho_{\hat{r}^{(n)}} - \rho_r\right)/\rho_r\right|$ were 1.4% $(n = 0)$, 0.22% $(n = 1)$, 0.03% $(n = 2)$, 0.005% $(n = 3)$, and $< 0.001\%$ $(n = 4)$. These results show that the number of iterations, $N = 4$, is sufficient for the SoS correction using Eq. (38). The parameters $\rho_{\widehat{r_B}}$, $\rho_{\hat{r}^{(n)}}$, $\widehat{d}^{(n)}$, and $\hat{r}^{(n)}$ required for SoS correction are obtained by directly calculating Eqs. (29), (34), (36), and (37), respectively, using $(\widehat{d_B}, \widehat{r_B})$ measured in procedure (III). Therefore, the construction of the B-mode image is not required in procedure (IV).

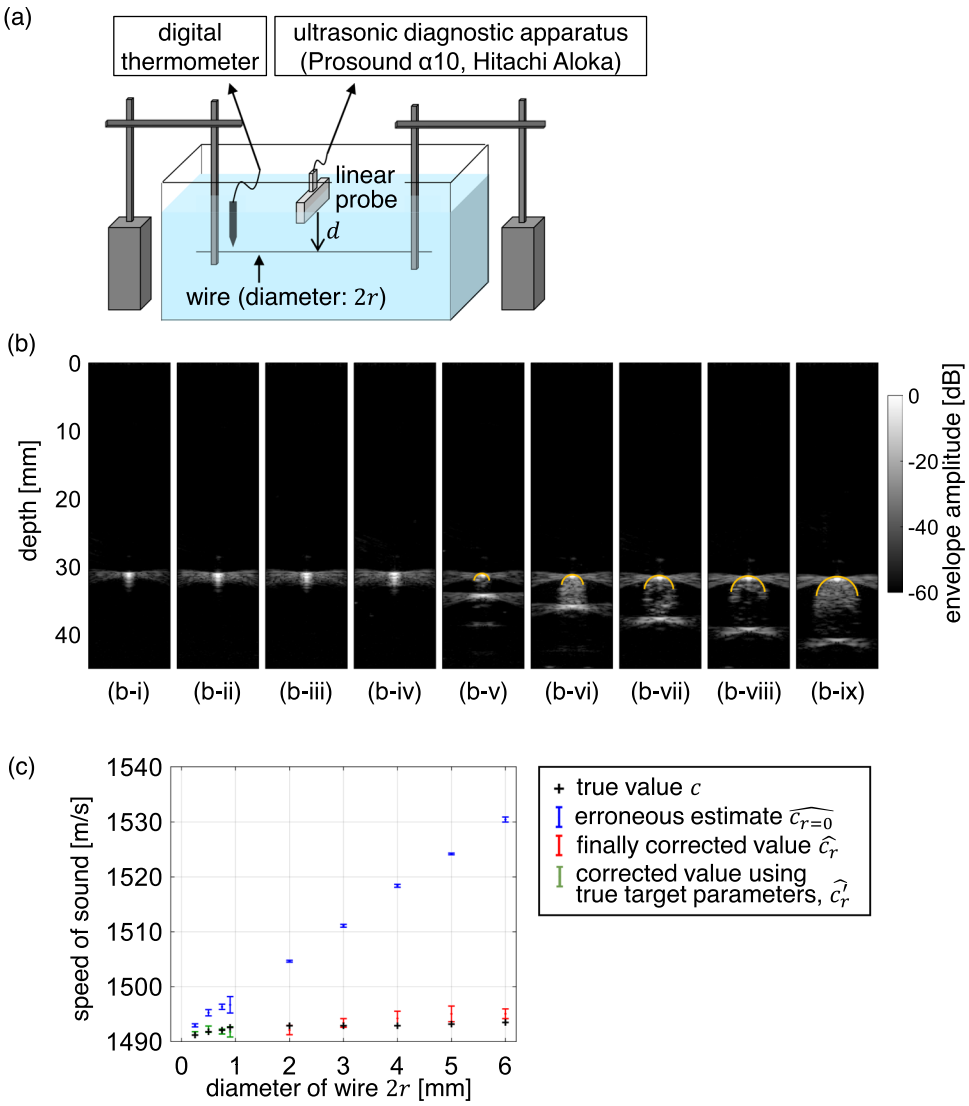

Fig. 7 **a** Experiment configuration for estimating the SoS in water using wires with several diameters as the targets. **b** B-mode images constructed with erroneously estimated SoS $\widehat{c_{r=0}}$ of (b-i) 1493, (b-ii) 1496, (b-iii) 1496, (b-iv) 1497, (b-v) 1505, (b-vi) 1511, (b-vii) 1519, (b-viii) 1524, and (b-ix) 1530 m/s for wires with diameters of (b-i) 0.25, (b-ii) 0.5, (b-iii) 0.75, (b-iv) 0.9, (b-v) 2, (b-vi) 3, (b-vii) 4, (b-viii) 5, and (b-ix) 6 mm, respectively. The measured target curvature radius $\widehat{r_B}$ was plotted at the measured depth $\widehat{d_B}$ on (b-v)–(b-ix) by the orange line. **c** Estimated results of SoS in water by: blue—conventional method using Eq. (7), $\widehat{c_{r=0}}$; red—proposed method using Eq. (38), $\widehat{c_r}$; green—$\widehat{c_r^{\prime}}$ which was corrected using the values of true wire diameter $2r$ and true SoS c in water instead of the measurement of $\widehat{r_B}$. The true SoS c was determined from the water temperature [21]

Experimental methods

The proposed method was applied to RF signals obtained from wires of several diameters arranged in a water tank. The SoS in water was estimated using RF signals obtained from the wire. The experimental configuration is shown in Fig. 7(a). The nylon wires with diameters of 0.25, 0.5, 0.75, and 0.9 mm and silicone rubber wires with diameters of 2, 3, 4, 5, and 6 mm were utilized as targets. Each wire was placed in a water tank such that the shallowest depth of the wire surface, d, was set at approximately 30 mm from the probe surface. The wire depth was set by moving the ultrasound probe using the manual stage with 0.1-mm resolution after contacting the probe surface and wire surface by observing the water tank and the B-mode image.

The cross-sectional view of the short axis of the wire was obtained using a linear array probe (UST-5412; Hitachi Aloka, Japan) connected to an ultrasonic diagnostic apparatus (Prosound α10; Hitachi Aloka, Japan). The transmitted and sampling frequencies were set at 7.5 and 40 MHz, respectively. The focal depth was set at 30 mm. The full widths at half maximum (FWHM) of the transmitted and

Table 1 Water temperature and true SoS determined from water temperature [21] in the experiment for each wire

Diameter of wire $2r$ [mm]	0.25	0.50	0.75	0.90	2	3	4	5	6
Water temperature [°C]	23.0	23.2	23.3	23.5	23.6	23.6	23.6	23.7	23.8
True SoS in water [m/s]	1491.2	1491.8	1492.1	1492.6	1492.9	1492.9	1492.9	1493.2	1493.5

received beams were 0.85 and 0.39 mm, respectively. The RF signals were acquired ten times for each wire by rearranging the wire. The true SoS in water was determined from the water temperature [21]. The water temperature was measured immediately before the measurement of each wire. The measured water temperature and true SoS determined from the measured water temperature are listed in Table 1.

The depth of the target surface observed on the B-mode image, $\widehat{d_{\mathrm{B}}}$, was estimated by measuring the received time of the wavefront of the beam-formed RF signal, $t\left(x_{\mathrm{beam}}\right)$, at $x_{\mathrm{beam}} = 0$, and by substituting $t\left(x_{\mathrm{beam}} = 0\right)$ into Eq. (24), and the resultant $\widehat{z_{\mathrm{B}}}\left(x_{\mathrm{beam}} = 0; \widehat{c_{r=0}}\right)$ into Eq. (25).

The target radius observed in the B-mode image, $\widehat{r_{\mathrm{B}}}$, was measured using a simple thresholding approach. After detecting the lateral positions of the target surface at several depths by applying the thresholding procedure to the beam-formed RF envelope amplitudes in the lateral direction, $\widehat{r_{\mathrm{B}}}$ was estimated using the least squares method. The threshold value was empirically determined. For wires with small diameters $2r \leq 0.9$ mm, we did not measure $\widehat{r_{\mathrm{B}}}$, because distinguishing whether the observed shape on the B-mode image showed the target shape or the shape of the PSF of ultrasound was difficult, which is discussed in the results section. Therefore, the SoS correction using the proposed method was applied to wires with large diameters $2r \geq 2$ mm.

For wires with small diameters $2r \leq 0.9$ mm, the theoretical value $r/(\widehat{c_{r=0}}/c)$ was used for $\widehat{r_{\mathrm{B}}}$ to discuss the feasibility of the proposed method if the target radius $\widehat{r_{\mathrm{B}}}$ was measurable from the B-mode image.

Results

Shape of target surface observed on the B-mode image

Figures 7(b-i)–7(b-ix) show the B-mode images constructed using the erroneously estimated SoS $\widehat{c_{r=0}}$ for wires with diameters of 0.25, 0.5, 0.75, 0.9, 2, 3, 4, 5, and 6 mm, respectively. The erroneously estimated SoS values $\widehat{c_{r=0}}$ used for the construction of the B-mode images were (b-i) 1493, (b-ii) 1496, (b-iii) 1496, (b-iv) 1497, (b-v) 1505, (b-vi) 1511 (b-vii) 1519, (b-viii) 1524, and (b-ix) 1530 m/s.

As shown in the B-mode images of wires with small diameters $2r \leq 0.9$ mm in Figs. 7(b-i)–7(b-iv), distinguishing the target shape from the shape of the PSF (FWHM: 0.39 mm in the lateral direction) is difficult. Thus, for wires with small diameters $2r \leq 0.9$ mm, we did not measure the radius $\widehat{r_{\mathrm{B}}}$ in the B-mode image.

For wires with large diameters $2r \geq 2$ mm, the measured target depth $\widehat{d_{\mathrm{B}}}$ and radius $\widehat{r_{\mathrm{B}}}$ (orange line) well corresponded to the shape of the target surface observed on the B-mode image, as shown in Figs. 7(b-v)–7(b-ix). The differences $\widehat{r_{\mathrm{B}}} - r/(\widehat{c_{r=0}}/c)$ between the measured curvature radii $\widehat{r_{\mathrm{B}}}$ on the B-mode image and theoretical values $r/(\widehat{c_{r=0}}/c)$ were 0.06 ± 0.06 mm (average $\pm$ standard deviation for ten measurements) for $2r = 2$ mm, 0.01 ± 0.06 mm for $2r = 3$ mm, -0.06 ± 0.10 mm for $2r = 4$ mm, -0.02 ± 0.11 mm for $2r = 5$ mm, and 0.03 ± 0.06 mm for $2r = 6$ mm.

SoS estimation

The results of the estimated SoS $\widehat{c_{r=0}}$ yielded by Eq. (7) of the conventional method (blue) and the final corrected SoS $\widehat{c_r}$ yielded by Eq. (38) of the proposed method (red) are shown in Fig. 7(c). The final corrected SoS values $\widehat{c_r}$, which were corrected without using the values of true target depth d and radius r, and true SoS c in water, are shown for wires with diameters $2r \geq 2$ mm. For wires with diameters $2r \leq 0.9$ mm, the corrected SoS values $\widehat{c_r'}$, which were corrected using the values of true wire diameter $2r$ and true SoS c in water instead of the measurement of $\widehat{r_{\mathrm{B}}}$, are plotted in green. The error bars show the average and standard deviation for ten measurements. The true SoS values c in water, measured from the water temperatures, are plotted as a black cross marker.

As shown in Fig. 7(c), SoS $\widehat{c_{r=0}}$ was overestimated using Eq. (7) of the conventional method. The positive error increased as the wire diameter increased, which coincided with the results of our previous study [7].

For wires with diameters $2r \leq 0.9$ mm, the estimation errors yielded by the conventional method, $\left|\widehat{c_{r=0}} - c\right|$, were at a maximum of 6 m/s. The errors $\left|\widehat{c_r'} - c\right|$ of the corrected SoS values $\widehat{c_r'}$ (green) were within 5 m/s. Thus, the improvement in the estimation error for the small target is not significant even if the target diameter is measurable on the B-mode image, while the bias error can be corrected by the SoS correction, as shown in Fig. 7(c).

For wires with diameters $2r \geq 2$ mm, the SoS estimation accuracy was significantly improved by the proposed method, whereas the standard deviation became larger than that of the conventional method owing to the measurement errors of the curvature radius $\widehat{r_{\mathrm{B}}}$ on the B-mode image. The absolute values of the estimation errors yielded by the conventional method, $\left|\widehat{c_{r=0}} - c\right|$, were a maximum of 38 m/s, and those yielded by the proposed method, $\left|\widehat{c_r} - c\right|$, were within 4 m/s. Thus, the proposed method considerably improved the SoS estimation accuracy, particularly for large targets.

Discussion

In this paper, SoS estimation method that considers the curvature radius r of the target surface was proposed and validated by means of a water tank experiment using a wire as a target. The method comprises four procedures: (I) to (IV). Procedure (II) requires only a quadratic polynomial approximation process, that is, the calculation of Eq. (7). Procedure (IV) requires iterative calculation of $\rho_{\widehat{r}^{(N)}}$ using Eq. (34). However, this calculation process can be omitted by preliminarily determining $\rho_{\widehat{r}^{(N)}}$ for each depth $\widehat{d_{\mathrm{B}}}$ and radius $\widehat{r_{\mathrm{B}}}$ and preparing a look-up table. Thus, procedures (II) and (IV) are clinically applicable.

Procedure (I) requires detection of the reception time of the wavefront of the received signal. In this study, a simple peak-detection method was used; however, the method should be modified for clinical applications to address the low signal-to-noise ratio and interference of scattered waves from the surrounding tissues in in vivo measurements.

Procedure (III) requires measuring the curvature radius $\widehat{r_{\mathrm{B}}}$ of the target in the B-mode image, as shown in Fig. 7(b). In the conducted experiment, measuring $\widehat{r_{\mathrm{B}}}$ from the B-mode image for small wires ($2r \leq 0.9$ mm) was difficult owing to the ultrasonic spatial resolution. Therefore, the proposed method was applied only to large wires ($2r \geq 2$ mm). As shown in Fig. 7(c), however, the SoS estimation error for the small targets ($2r \leq 0.9$ mm) was at a maximum of 6 m/s without correction of the target size using the proposed method. These results show that the SoS correction using the proposed method should be applied to a large target whose observed radius $\widehat{r_{\mathrm{B}}}$ on the B-mode image is measurable, whereas the conventional SoS estimation assuming an ideal point scatterer is applicable to smaller targets. As shown by the green plots in Fig. 7(c), the bias error of the SoS estimates for small targets ($2r \leq 0.9$ mm) can be improved with the proposed method if the target radius $\widehat{r_{\mathrm{B}}}$ is measurable on the B-mode image. Improvement of the ultrasonic spatial resolution and/or development of a measurement method of $\widehat{r_{\mathrm{B}}}$ for small targets will enable the application of the proposed method to small targets and improve the bias error of the SoS estimates.

As shown in Fig. 7(c), the standard deviation of the estimated SoS values increased more for the proposed method than for the conventional method, whereas the bias error was significantly improved by the proposed method. In this study, a simple threshold procedure was used to measure the target radius $\widehat{r_{\mathrm{B}}}$ on the B-mode image. Improvement of the measurement method for $\widehat{r_{\mathrm{B}}}$ will contribute to the accurate SoS estimation by the proposed method.

In the experiment using wires, the estimated SoS $\widehat{c_r}$ yielded by the proposed method was slightly overestimated for the large wires, as shown by the red plots in Fig. 7(c). A possible reason for this is the slight mismatch between the actual target depth and the focal depth. If there are systematic errors for the arranged target depth, the approximation error of the focused beam as a plane wave within the transmitted beam width w_{beam} around the focal depth d may cause a systematic error in the estimated SoS; therefore, detailed examination is required in a future study.

In this study, the target was assumed to be located exactly below the center element. In an actual case, the target may not exist exactly below the center element; however, the maximum difference in lateral positions between the center element and target is half of the element pitch (0.1 mm in this study) by selecting the proper analysis beam. To validate the feasibility of this assumption, we theoretically evaluated the SoS estimation error when the lateral position of the ideal point scatterer deviated 0.1 mm from the lateral position of the center element. We theoretically calculated the propagation time distribution and estimated the SoS using Eq. (7) for several target depths d. We found that the SoS estimation errors were 0.0001% for $d = 30$ mm, 0.003% for $d = 5$ mm, and 0.023% for $d = 1$ mm. Thus, we confirmed that the approximation for the target lateral position does not affect the SoS estimation.

As a fundamental study, the transmitted wave was assumed to be focused on the target surface to approximate the focused wave as a plane wave around the focal region. However, focusing on all target surfaces is difficult in actual measurements; therefore, examining the effect of the difference between the target surface depth and beam-focused depth in the proposed method is necessary. Alternatively, the transmission of plane waves enables the application of the proposed method to the targets irrespective of their depths, while it causes different concerns, such as a low signal-to-noise ratio and interference of scattered waves from the surrounding tissues.

As described in the Introduction, many SoS estimation approaches assume that the scattering source is an ideal point scatterer. In these methods, the SoS is overestimated if the target used for the SoS estimation has a non-negligible size. When the estimated SoS is directly used for diagnosis, this overestimated SoS $\widehat{c_{r=0}}$ results in a false diagnosis; therefore, SoS correction using the proposed method is essential.

When an overestimated SoS $\widehat{c_{r=0}}$ is used only for the received beamforming at the target position, it does not negatively affect the focusing quality, because the propagation time at each element does not change between the true condition $T_{\mathrm{fb}}\left(x_k;c,d,r\right)$ and the erroneously estimated condition $T_{\mathrm{fb}}\left(x_k;\widehat{c_{r=0}},\widehat{d_{r=0}},r=0\right)$, that is, the element signals can be in-

phase using the time delay $T_{\mathrm{fb}}\left(x_k;\widehat{c_{r=0}},\widehat{d_{r=0}},r=0\right)$ obtained from the erroneously estimated condition. However, when overestimated SoS $\widehat{c_{r=0}}$ is used for the received beamforming at different positions, the element signals basically cannot be in-phase using the time delay $T_{\mathrm{fb}}\left(x_k;\widehat{c_{r=0}},\widehat{d_{r=0}},r=0\right)$, which is obtained from the erroneously estimated condition, because the time delay does not correspond to the true propagation time, which degenerates the focusing quality. Thus, when the estimated SoS is used for received beamforming at other positions, the effect of the target size must be corrected.

Thus, in the time-delay-based SoS estimation method, the effect of target size must be carefully considered according to the intended application of the estimated SoS value.

Conclusions

We herein proposed an estimation method for SoS in a propagation medium that is applicable to a signal received from a target of finite size. The proposed method can estimate the SoS without information on the true depth and size of the target and the true SoS. In the experiment using wires with several diameters as targets, the proposed method significantly decreased the maximum SoS estimation error from 38 m/s to 6 m/s. The application of this method to in vivo measurements will be the subject of our future work.

Supplementary Information The online version contains supplementary material available at https://doi.org/10.1007/s10396-023-01282-2.

Acknowledgements This work was partly supported by the Japan Society for the Promotion of Science KAKENHI Grant 21K14166.

Data availability The data are available from the corresponding author upon reasonable request.

Declarations

Conflict of interest Shohei Mori, Hiroshi Kanai, and Mototaka Arakawa declare no conflicts of interest.

Ethical approval This article does not contain any studies involving human or animal subjects performed by any of the authors.

References

1. Ormachea J, Parker KJ. A preliminary study of liver fat quantification using reported ultrasound speed of sound and attenuation parameters. Ultrasound Med Biol. 2022;48:675–84.
2. Robinson DE, Chen F, Wilson LS. Measurement of velocity of propagation from ultrasonic pulse-echo data. Ultrasound Med Biol. 1982;8:413–5,417–20.
3. Ophir J. Estimation of the speed of ultrasound propagation in biological tissues: a beam-tracking method. IEEE Trans Ultrason Ferroelectr Freq Control. 1986;33:359–68.
4. Anderson ME, Trahey GE. The direct estimation of sound speed using pulse-echo ultrasound. J Acoust Soc Am. 1998;104:3099–106.
5. Jakovljevic M, Hsieh S, Ali R, Kung GCL, Hyun D, Dahl JJ. Local speed of sound estimation in tissue using pulse-echo ultrasound: Model-based approach. J Acoust Soc Am. 2018;144:254–66.
6. Abe K, Arakawa M, Kanai H. Estimation method for sound velocity distribution for high-resolution ultrasonic tomographic imaging. J Med Ultrason. 2019;46:27–33.
7. Nakayama A, Mori S, Arakawa M, Kanai H. Estimation error in sound velocity depending on size of target scatterer. Jpn J Appl Phys. 2021;60:SDDE17-1–6.
8. Mori S, Nakayama A, Onoda K, Arakawa M, Kanai H. Preliminary study on estimation of speed of sound in propagation medium considering target scatterer size. Proc IEEE Int Ultrason Symp. 2021. https://doi.org/10.1109/IUS52206.2021.9593638.
9. Hayashi N, Tamaki N, Senda M, Yamamoto K, Yonekura Y, Torizuka K, Ogawa T, Katakura K, Umemura C, Kodama M. A new method of measuring in vivo sound speed in the reflection mode. J Clin Ultrasound. 1988;16:87–93.
10. Napolitano D, Chou CH, McLaughlin G, Ji TL, Mo L, DeBusschere D, Steins R. Sound speed correction in ultrasound imaging. Ultrasonics. 2006;44:e43–6.
11. Nitta N, Washio T. Relation between statistical properties of sound speed distribution and average sound speed estimation. Jpn J Appl Phys. 2021;60:SDDE18-1–13.
12. Nitta N, Washio T, Numano T. Basic investigation on identification of tissue composition based on propagation speeds of longitudinal and shear waves. Jpn J Appl Phys. 2022;61:SG1023-1–8.
13. Imbault M, Faccinetto A, Osmanski BF, Tissier A, Deffieux T, Gennisson JL, Vilgrain V, Tanter M. Robust sound speed estimation for ultrasound-based hepatic steatosis assessment. Phys Med Biol. 2017;62:3582–98.
14. Imbault M, Dioguardi Burgio M, Faccinetto A, Ronot M, Bendjador H, Deffieux T, Triquet EO, Rautou PE, Castera L, Gennisson JL, Vilgrain V, Tanter M. Ultrasonic fat fraction quantification using in vivo adaptive sound speed estimation. Phys Med Biol. 2018;63:215013.
15. Hasegawa H, Nagaoka R. Initial phantom study on estimation of speed of sound in medium using coherence among received echo signals. J Med Ultrason. 2019;46:297–307.
16. Sannou F, Nagaoka R, Hasegawa H. Estimation of speed of sound using coherence factor and signal-to-noise ratio for improvement of performance of ultrasonic beamformer. Jpn J Appl Phys. 2020;59:SKKE14-1–10.
17. Nagaoka R, Yoshizawa S, Umemura S, Hasegawa H. Effects from correction of speed of sound in transmit and receive beamforming using focus beam. Jpn J Appl Phys. 2021;60:SDDE19-1–12.
18. Ali R, Telichko AV, Wang H, Sukumar UK, Vilches-Moure JG, Paulmurugan R, Dahl JJ. Local sound speed estimation for pulse-echo ultrasound in layered media. IEEE Trans Ultrason Ferroelectr Freq Control. 2022;69:500–11.
19. Stähli P, Kuriakose M, Frenz M, Jaeger M. Improved forward model for quantitative pulse-echo speed-of-sound imaging. Ultrasonics. 2020;108:106168.
20. Chen CF, Robinson DE, Wilson LS, Griffiths KA, Manoharan A, Doust BD. Clinical sound speed measurement in liver and spleen in vivo. Ultrason Imaging. 1987;9:221–35.

21. Kroebel W, Mahrt KH. Recent results of absolute sound velocity measurements in pure water and sea water at atmospheric pressure. Acta Acust United Acust. 1976;35:154–64.